This is a postprint version of the following published document:

Alba Rodriguez Lorente; Andres Barrado Bautista; Carlos Alberto Calderon Benavente; Cristina Fernandez Herrero; Antonio Lazaro Blanco (2020).

Non-inverting and Non-isolated Magnetically Coupled Buck-Boost Bidirectional DC-DC Converter

Non-Inverting and Non-Isolated Magnetically Coupled Buck-Boost Bidirectional DC-DC Converter

Alba Rodríguez-Lorente, Andrés Barrado, Carlos Calderón, Cristina Fernández, and Antonio Lázaro
Power Electronics Systems Group, Universidad Carlos III de Madrid
e-mail: alba.rodriguez@uc3m.es; andres.barrado@uc3m.es

Abstract- **A new non-isolated DC-DC converter with non-inverting output and buck-boost operation, named Magnetically Coupled Buck-Boost Bidirectional converter (MCB³), is presented in this paper. The MCB³ passive components arrangement connects the input and output ports getting an equivalent behavior to that of the Dual Active Bridge (DAB) converter, but in a non-isolated topology. This equivalency allows applying Triple Phase Shift (TPS) modulation to MCB³. TPS is known to minimize conduction losses and to achieve soft-switching at any load in the DAB converter. Throughout the paper, the features of the DAB converter are used as a reference to show the main features of the proposed converter. Moreover, other modulation strategies based on TPS modulation are used in MCB³ to operate within the minimum losses path.The multiple operation modes found on the MCB³ under TPS modulation are identified, classified, and used to find the operating points that minimize the switching and conduction losses over the power range. The analysis is shown for the boost mode that is the worst-case design. MCB³ and DAB topologies are designed and simulated for the same specification to validate the theoretical study. Finally, experimental measurements on 460W-prototypes for both topologies corroborate the equivalent operation and the main features of the MCB³.**

I. INTRODUCTION

A non-isolated bidirectional DC-DC energy transfer capability with a buck-boost operation is useful in many power conversion systems and applications, such as photovoltaic systems, DC microgrids, or electric transport [1]–[5], as long as galvanic isolation is not necessary for high-level safety reasons. The energy storage systems included must ensure the continuity of the power supplied to the output in all circumstances, regardless of the input voltage and the transfer direction.

Within the alternatives with non-inverting output, bidirectional SEPIC/ZETA converter is an attractive choice, with little input and output current ripple and simple arrangement. However, it has a high passive component count that can be even higher to reduce switching losses, or need of frequency variation [6], [7]. Four Switches Non-inverting Buck-Boost converter (FSBB) with two half-bridges and a single inductor, is an interesting choice within the same application area. The higher number of MOSFETs compared to simpler topologies, allows soft-switching operation without adding extra components, in exchange for increased control complexity [8], [9]. Several phases of FSBB are considered in [9] to increase efficiency.Also, more recent topologies, as shown in [10], are investigating FSBB modifications to achieve soft-switching operation. Transformerless Dual Active Half-Bridge (TLDAB), in [11], has been developed based on a modification of the well-known Dual Active Bridge converter [12]. TLDAB converter employs AC power transfer to substantially reduce the energy storage requirement in the magnetic components, which directly impacts the overall power density of the entire system. However, the TLDAB converter requires of variable switching frequency and mandatory snubbers to achieve the soft switching operation goal.

The commented topologies are summarized in TABLE I, with additional information regarding the number and type of components, and the efficiency at the referred voltage gain.

To reduce the overall losses with no need for extra component nor frequency variation, and a desirable reduction on the magnetics volume, the Magnetically Coupled Bidirectional Buck-Boost converter (MCB³) is proposed.

The MCB³ converter provides non-inverting non-isolated buck-boost bidirectional features, with a passive component arrangement that forces the current to follow a specific path in an AC power transfer. The proposed passive link of the input and output ports makes the MCB³ operation analogous to that of the traditional Dual Active Bridge converter. This achieved behavioral equivalence makes the MCB³ controllable by employing advanced modulation strategies proven to achieve the target features in the DAB converter. In particular, the Triple Phase Shift modulation (TPS) [13], [14], is chosen in this paper to obtain soft-switching operation at a fixed frequency in all the MOSFETs of the MCB³. Additionally, minimum conduction losses can be achieved for the entire power range. Moreover, AC power transfer is exploited to save volume on the magnetic components.

The rest of the paper is organized as follows: the MCB³ converter derivation and operating principle are explained in Section II. The different operation possibilities regarding the use of Triple Phase Shift modulation are classified in Section III, together with the procedure to derive the rms current expressions in steady-state operation. In Section IV, the power losses reduction mechanisms applied are discussed, involving soft-switching operation and conduction losses minimization. In Section V, the volts·second in the windings of the magnetic coupling component are studied to size the magnetizing inductance value, so the operation remains close to the ideal one. Simulation and experimental results for the worst-case design scenario are presented in Section VI, along with the results obtained for a DAB prototype for the same specification, to validate both the feasibility of the proposal and the hypothesis of behavioral equivalency between them. The conclusions of the research are given in Section VII.

TABLE I
SUMMARY OF THE CONSIDERED DC-DC NON ISOLATED BUCK-BOOST TOPOLOGIES

Topology	MOSFETs	Passive Components (of which magnetics)	Soft Switching	Control Flexibility	Efficiency	Voltage gain (Boost operation)
SEPIC/ZETA *w/extra comp.* [6]	4	7 (3)	Yes	Low	90%	2.01
SEPIC/ZETA [7]	2	3(2)	Yes [1]	Low	90%	2.67
FSBB [9]	4 [2]	1 (1) [2]	Yes	Medium	96% [2]	2
ZVS-NIBB [10]	4	9 (3)	Yes	Low	94%	1
TLDAB [11]	8	4 (2)	Yes [1]	Low	82.5%	3.6

[1] Variable frequency [2] Referred to single-phase module

II. TOPOLOGY DERIVATION AND BASIC OPERATION PRINCIPLE

The circuit of the proposed MCB[3] converter is shown in Fig. 1. The power stage includes two full-bridges (Bridge 1 and Bridge 2), which generate two AC differential signals (v_{11} and v_{22}) and an *AC-link*, comprising the main passive components. This *AC link* is composed of two series capacitors C_1 and C_2 to block the DC component in the *AC-link,* and a coupled inductor, *CI*, which manages and transfers the power between the two bridges. Providing a strong magnetic coupling in the *CI* windings and the location of the corresponding terminals, the current through the upper branch of the *AC-link*, i_{L1}, will have the same value and opposite sign to that through the lower branch, i_{L2}, resulting in no return current through the ground line between the two bridges. The way the *CI,* along with the blocking capacitors connects the input and output full bridges, produces an analogous operation to the AC-link in the traditional Dual Active Bridge converter (DAB) [12], Fig. 2. Although traditionally the DAB converter is represented with a single inductor, in Fig. 2 it has been split in L_1 and L_2 to ease the comparison of the two topologies.
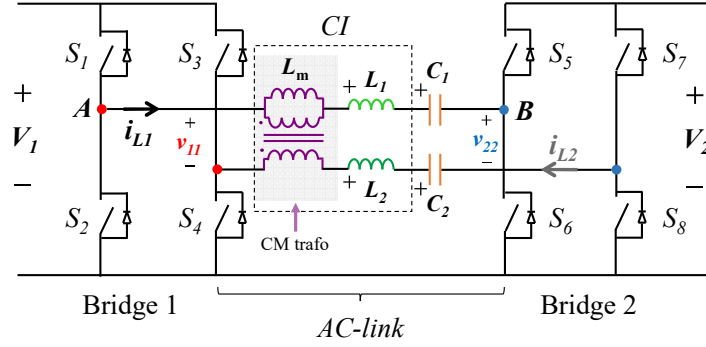

Fig. 1 Proposed Magnetically Coupled Buck-Boost Bidirectional converter
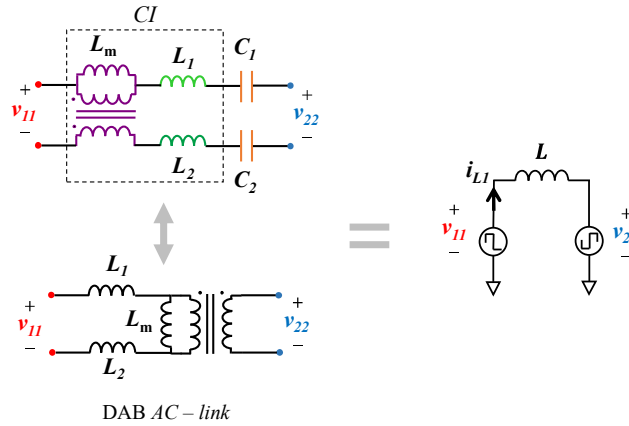

Fig. 2 *AC-links* of MCB[3] and DAB converters and simplified circuit

Unless otherwise specified, to ease the theoretical analysis discussed in this paper, coupled inductor, *CI,* is decomposed into a Common Mode (CM) transformer, with turns ratio equal to 1, and two discrete inductors L_1 and L_2. The equations of the voltages in *AC-link* components are shown in (1) to (3). The value of the capacitors equal ($C_1 = C_2$) and assumed to be large enough to consider constant the voltage across them. The value of magnetizing inductance L_m of the CM transformer is considered as infinite to recreate an ideal coupling.

$$v_T = v_A - v_B - (v_{L1} + V_{C1}) \qquad (1)$$
$$v_{L1} = v_{L2} = (v_{11} - v_{22})/2 \qquad (2)$$
$$V_{C1} = (V_1 - V_2)/2 \qquad (3)$$

Analyzing the circuit, as ideally, i_{L1} equals i_{L2}, the voltages across C_1 and C_2 cancel each other as well as the voltages in the primary and secondary windings of the CM transformer, as the turn ratio is 1. Hence, the voltage across the inductors only depends on the differential voltages v_{11} and v_{22}. Besides, by considering a strong coupling, inductors L_1 and L_2 act as whether they were in series, hence forming an equivalent inductor, L, with the value equal to the sum of them. Fig. 2 (b) represents the simplified version of the described operation, reducing all the *AC-link* passive components to an only inductor, L. From this analysis, it is deduced that the operation of the MCB^3 converter is mainly based on the AC energy transference from one bridge to the other throughout a strongly inductive impedance (represented by L), as a consequence of the voltage differences applied between its terminals.

Notice that the proposed converter acts as a current source. Therefore, the voltage gain is settled indirectly by the current transferred from the input to the output port.

III. STEADY-STATE ANALYSIS WITH TRIPLE PHASE SHIFT

As said, the operation of the proposed converter depends mainly on the differential voltages created by the full-bridges' operation. As the simplified structure, as well as the operation, reminds of that of the well-known Dual Active Bridge converter (DAB) [12], advanced control strategies proven to enhance the DAB features, can be taken into consideration to drive MCB^3.

Among the DAB converter control strategies in the literature, Phase Shift is the most straightforward scheme to be used.

In PS modulation, duty cycles D_1 and D_2 are set to 1, $T_{sw}/2$, being D_1 the Bridge 1 duty cycle defined on the differential signal v_{11}. Equivalently D_2 is the Bridge 2 duty cycle defined on v_{22}, Fig. 3 [16].
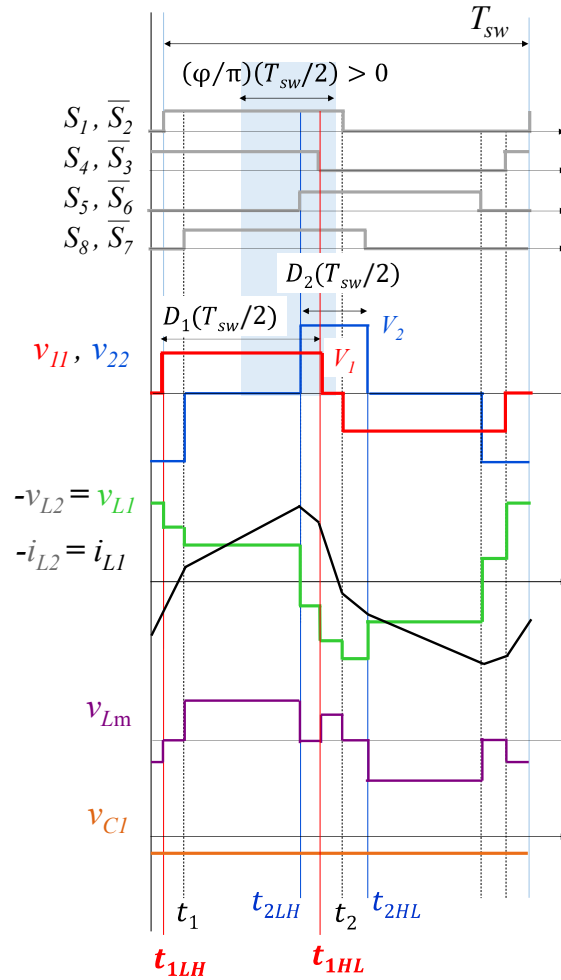

Fig. 3 MCB^3 converter steady-state waveforms in boost operation with TPS

The two legs in each full-bridge, are 180° shifted.

The phase shift between MOSFETs S_1-S_2 (outer leg of Bridge 1) and S_5-S_6 (inner leg of Bridge 2) or, equivalently, the angle φ (in radians) between differential voltages v_{11} and v_{22}, is the only control parameter in the PS modulation. This phase shift angle, φ, is then in charge of control the power transfer, and the transfer direction from Bridge 1 to Bridge 2 when φ is positive, and from Bridge 2 to Bridge 1 when it is negative. However, the performance of the PS is reduced when the ratio V_2/V_1 differs from 1 [12] as the soft-switching operation is lost at light load.

Triple Phase Shift modulation (TPS) fixes some issues of PS control strategy, acting on up to three control parameters (D_1, D_2, and φ) to improve the controllability of the converter. TPS modulation extends the soft-switching region to the whole power range independently of the ratio V_2/V_1 and allows to minimize the rms current demand by adequately shaping the inductor current profile [13]–[15]. For the reasons given, TPS modulation is chosen to drive the proposed converter.

Fig. 3 shows the main steady-state waveforms for a generic TPS operating point in the proposed MCB³ converter. Driving signals are shown in grey; differential voltages v_{11} and v_{22} in blue and red respectively; inductor L_1 voltage and current in green and black; CM transformer voltage current in purple, and C_1 voltage in orange. Neither dead-time nor losses are considered in the representation. Driving signals with a top bar are complementary to the real driving signal.

The possible scenarios that appear when combining voltages V_1 and V_2, with the duty cycles D_1 and D_2, were classified in [16] for the DAB converter with TPS modulation. The same classification criterion is used for the MCB³: *Case* 1 if $V_1 \geq V_2$ & $D_1 > D_2$; *Case* 2 if $V_1 \geq V_2$ & $D_1 \leq D_2$; *Case* 3 if $V_1 < V_2$ & $D_1 > D_2$ and *Case* 4 if $V_1 < V_2$ & $D_1 \leq D_2$. Notice that the change from *Case* 1 to *Case* 4, and from *Case* 2 to *Case* 3 is easily done when needed, by changing duty cycles as appropriate.

This paper analyses MCB³ boost operation in *Case* 3, and Bridge 1 to Bridge 2 transfer. Boost operation represents the worst-case design with a higher circulating current than equivalent buck operation for a given load. Within the boost operation alternatives, *Case* 3 is preferred as it allows soft-switching operation in the whole power range (explanation in Section IV).

As seen in Fig. 3, when an edge appears on signals v_{11} and v_{22}, the slope in the inductor current waveform changes. The way these slopes change produces up to fourteen current profiles, named Switching Modes. These fourteen Switching Modes (SM) are identified in [16] for the DAB converter as well, through the progressive increase of the angle φ from -π to π. Seven each direction. The same Switching Modes have appeared once applied the described identification procedure to the analyzed MCB³ converter. The seven SM found within the direction considered, are named as SM_1, SM_2, SM_3, SM_4, SM_5, SM_2^* and SM_3^*. Switching Modes SM_2^* and SM_3^* occur for $D_1 \geq 1$-D_2 in *Case* 1 and 2, or $D_2 \geq 1$-D_1 in *Case* 3 and 4. Their non-asterisked homonyms occur for $D_1 \leq 1$-D_2. Fig. 4 depicts the seven Switching Modes for *Case* 3 and positive φ.

Every Switching Mode found has its output power definition. TABLE II shows the angle φ range for each Switching Mode and the corresponding power expression. According to the SM ranges in TABLE II, the operating point represented in Fig. 3 is classified as SM_3^*.

Different rms current expressions exist for every SM. TABLE III shows the i_{L1} current expression at the *Reference switching instants*, which are those time instants that delimit the duty cycles D_1 (t_{1LH} and t_{1HL}) and D_2 (t_{2LH} and t_{2HL}).
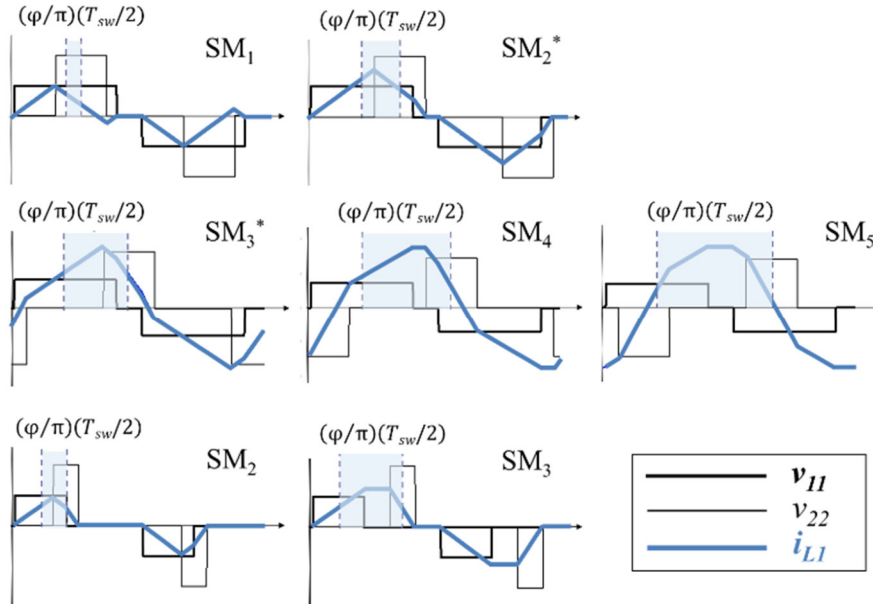

Fig. 4 Example of the Switching Modes current profiles for $0<\varphi<\pi$

TABLE II
SWITCHING MODE RANGE AND POWER EXPRESSIONS IN CASE 3

SM	Range	Power
SM_1	$\left(0, \dfrac{D_1 - D_2}{2/\pi}\right]$	$\dfrac{V_1 \cdot V_2 \cdot D_2(\varphi/\pi)}{2 \cdot f_{sw} \cdot L}$
SM_2	$\left(\dfrac{D_1 - D_2}{2/\pi}, \dfrac{D_1 + D_2}{2/\pi}\right]$	$\dfrac{V_1 \cdot V_2 \cdot D_2}{4 f_{sw} \cdot L}\left(\dfrac{\varphi}{\pi}\left(-D_1 - D_2 + \dfrac{\varphi}{\pi}\right)\right.$
SM_2*	$\left(\dfrac{D_1 - D_2}{2/\pi}, 1 - \dfrac{D_1 + D_2}{2/\pi}\right]$	$\left. + \dfrac{(D_1 - D_2)^2}{4}\right)$
SM_3	$\left(\dfrac{D_1 + D_2}{2/\pi}, 1 - \dfrac{D_1 + D_2}{2/\pi}\right]$	$\dfrac{V_1 \cdot V_2 \cdot D_2 \cdot D_1}{4 \cdot f_{sw} \cdot L}$
SM_3*	$\left(1 - \dfrac{D_1 + D_2}{2/\pi}, \dfrac{D_1 + D_2}{2/\pi}\right]$	$\dfrac{V_1 \cdot V_2 \cdot D_2}{2 f_{sw} \cdot L}\left(\dfrac{\varphi}{\pi}\left(1 - \dfrac{\varphi}{\pi}\right)\right.$ $\left. - \dfrac{(D_1 - 1)^2 + (D_2 - 1)^2}{4}\right)$
SM_4	$\left(1 - \dfrac{D_1 + D_2}{2/\pi}, 1 - \dfrac{D_1 - D_2}{2/\pi}\right]$	$\dfrac{V_1 \cdot V_2 \cdot D_2}{2 f_{sw} \cdot L}\left(\dfrac{\varphi}{\pi}\left(D_1 + D_2 + \dfrac{\varphi}{\pi} - 1\right)\right.$ $\left. - \dfrac{(D_1 - D_2)^2}{4}\right)$
SM_5	$\left(1 - \dfrac{D_1 - D_2}{2/\pi}, 1\right]$	$\dfrac{V_1 \cdot V_2 \cdot D_2(1 - (\varphi/\pi))}{2 f_{sw} \cdot L}$

Equations (4) to (7) define the *Reference switching instants* based on the control parameters of TPS modulation.

$$t_{1LH} = T_{sw} \cdot (1 - D_1)/4 \qquad (4)$$

$$t_{1HL} = T_{sw} \cdot (1 + D_1)/4 \qquad (5)$$

$$t_{2LH} = T_{sw} \cdot (2\varphi/\pi + 1 - D_2)/4 \qquad (6)$$

$$t_{2HL} = T_{sw} \cdot (2\varphi/\pi + 1 + D_2)/4 \qquad (7)$$

The first four switching instants appearing from the beginning of the period are enough to describe the complete waveform since it is symmetrical. If the needed switching instants do not match with any of the *Reference switching instants*, it is possible to obtain the required instant as a linear combination from them (e.g., in Fig. 3, t_1 would be equivalent to t_{2HL} - $T_{sw}/2$, and t_2 as $t_{1LH} + T_{sw}/2$).

The given index to the *Reference switching instants* is intended to identify them in any waveform along this paper, as this index defines the change produced in waveforms v_{11} or v_{22} (e.g., in t_{1LH}, number 1 means that it defines a change in waveform v_{11}, and LH refers to the Low-to-High edge in the positive half of the v_{11} waveform).

From the information in TABLE II, the i_{L1rms} current is obtained with (8). To found it systematically, t_{ini}, must be replaced by the first rising edge time that occurred for v_{11} or v_{22}, during the first half period. t_{half} must be replaced by the fourth switching instant of v_{11} or v_{22} from the previously settled t_{ini}. The time-lapse between t_{ini} and t_{half} describe a half period of the current waveform. The procedure includes the partial integration of the instantaneous current. An example of this procedure applied to i_{L1} in Fig. 3 is shown in (9)).

TABLE III
INSTANTANEOUS CURRENT EXPRESSIONS IN CASE 3

SM	Current
SM$_1$	$i_{L1}(t_{1LH}) = -i_{L1}(t_{1HL}) = -\dfrac{D_1 \cdot V_1 - D_2 \cdot V_2}{4f_{sw} \cdot L}$ $i_{L1}(t_{2LH}) = \dfrac{D_2 \cdot V_1 + 2V_1(\varphi/\pi) - D_2 \cdot V_2}{4f_{sw} \cdot L}$ $i_{L1}(t_{2HL}) = -\dfrac{D_2 \cdot V_1 - 2V_1(\varphi/\pi) - D_2 \cdot V_2}{4f_{sw} \cdot L}$
SM$_2$ and SM$_{2*}$	$i_{L1}(t_{1LH}) = -i_{L1}(t_{2HL}) = \dfrac{D_1 \cdot V_1 - D_2 \cdot V_2}{4f_{sw} \cdot L}$ $i_{L1}(t_{2LH}) = \dfrac{D_1 \cdot V_1 + 2V_2(\varphi/\pi) - D_1 \cdot V_2}{4f_{sw} \cdot L}$ $i_{L1}(t_{1HL}) = \dfrac{D_2 \cdot V_1 - 2V_1(\varphi/\pi) - D_2 \cdot V_2}{4f_{sw} \cdot L}$
SM$_3$	$i_{L1}(t_{1LH}) = -i_{L1}(t_{2HL}) = -\dfrac{D_1 \cdot V_1 - D_2 \cdot V_2}{4f_{sw} \cdot L}$ $i_{L1}(t_{1HL}) = i_{L1}(t_{2LH}) = \dfrac{D_2 \cdot V_2 + D_1 \cdot V_1}{4f_{sw} \cdot L}$
SM$_{3*}$	$i_{L1}(t_{1LH}) = -\dfrac{D_1 \cdot V_2 - 2V_2(1 - (\varphi/\pi)) + D_1 \cdot V_1}{4f_{sw} \cdot L}$ $i_{L1}(t_{1HL}) = \dfrac{D_2 \cdot V_1 + 2V_2(\varphi/\pi) - D_1 \cdot V_2}{4f_{sw} \cdot L}$ $i_{L1}(t_{2LH}) = \dfrac{D_2 \cdot V_1 + 2V_1(\varphi/\pi) - D_2 \cdot V_2}{4f_{sw} \cdot L}$ $i_{L1}\left(t_{2LH} - \dfrac{T_{sw}}{2}\right) = \dfrac{D_2 \cdot V_1 - 2V_1(1 - (\varphi/\pi)) + D_2 \cdot V_1}{4f_{sw} \cdot L}$
SM$_4$	$i_{L1}(t_{1HL}) = i_{L1}(t_{2LH}) = \dfrac{D_2 \cdot V_2 + D_1 \cdot V_1}{4f_{sw} \cdot L}$ $i_{L1}(t_{1LH}) = -\dfrac{D_1 \cdot V_2 - 2V_2\left(1 - \left(\dfrac{\varphi}{\pi}\right)\right) + D_1 \cdot V_1}{4f_{sw} \cdot L}$ $i_{L1}\left(t_{2HL} - \dfrac{T_{sw}}{2}\right) = \dfrac{D_2 \cdot V_2 + 2V_1(1 - (\varphi/\pi)) - D_2 \cdot V_1}{4f_{sw} \cdot L}$
SM$_5$	$i_{L1}(t_{1LH}) = -i_{L1}(t_{1HL}) = -\dfrac{D_2 \cdot V_2 + D_1 \cdot V_1}{4f_{sw} \cdot L}$ $i_{L1}\left(t_{2LH} - \dfrac{T_{sw}}{2}\right) = -\dfrac{D_2 \cdot V_2 + 2V_1(1 - (\varphi/\pi)) + D_2 \cdot V_1}{4f_{sw} \cdot L}$ $i_{L1}\left(t_{2HL} - \dfrac{T_{sw}}{2}\right) = \dfrac{D_2 \cdot V_2 - 2V_1(1 - (\varphi/\pi)) - D_2 \cdot V_1}{4f_{sw} \cdot L}$

$$i_{L1\,rms}{}^2 = \frac{2}{T_{sw}} \int_{t_{ini}}^{t_{half}} i_{L1}(t)^2 dt \qquad (8)$$

$$i_{L1\,rms}{}^2 = \frac{2}{T_{sw}} \int_{t_{1LH}}^{t_2} i_{L1}(t)^2 dt = \frac{2}{T_{sw}}\left(\int_{t_{1LH}}^{t_1} i_{L1}(t)^2 dt + \int_{t_1}^{t_{2LH}} i_{L1}(t)^2 dt + \int_{t_{2LH}}^{t_{1HL}} i_{L1}(t)^2 dt + \int_{t_{1HL}}^{t_2} i_{L1}(t)^2 dt \right) \qquad (9)$$

IV. LOSSES MINIMIZATION MECHANISMS

In this section, the different mechanisms involving losses minimization in the proposed converter are discussed, exploiting TPS modulation. The goal is to simultaneously reduce the switching and the conduction losses, without the need for frequency variation nor added components.

The traditional DAB converter is commonly designed so that the input-output voltage ratio matches the transformer turn ratio, thus achieving ZVS operation [12]. However, according to [16], the appliance of (10) allows for soft-switching operation regardless of the turns ratio, n, for any load. Then, n becomes an extra freedom degree.

$$D_1 \cdot V_1 \cdot n = D_2 \cdot V_2 \qquad (10)$$

Once more, since the MCB³ structure and operation principle allows for taking advantage of the strengths of the DAB advanced modulation strategies, the application of (10) achieves soft-switching operation in the proposed converter. In *Case 3* (Boost operation) described, (10) is met in the MCB³ converter providing n equals 1.

The modulation strategy used to drive the proposed MCB³ converter, starts with $D_1 = D_2 = 0$, for any phase shift φ. D_1 value is gradually increased from 0 to 1. D_2 is then obtained with D_1 and (10). According to the proposals in [13], [15], once $D_1 = 1$, it remains set to 1, and only D_2 is variated. The resultant TPS modulation pattern is equivalent to the Extended Phase Shift modulation [17], [18]. From that set-point, following with the gradual increase of D_2, eventually, it will also reach 1, from when the control only will vary φ. This last TPS pattern recreates traditional PS modulation [12]. As both EPS and PS modulation are particularizations of TPS, then the expressions in TABLE II and TABLE III are valid for all the three modulation schemes.

Fig. 5 shows the seven Switching Mode areas for a given V_1/V_2 ratio, as a function of φ and D_2. The duty cycle D_1 is deduced from (10) if D_2 is lower than (V_1/V_2), or equal to 1 otherwise.

For any combination of D_1-D_2-φ, a value of power P_o, and RMS current i_{L1} are obtained, by substituting the three variables considered into the corresponding equations.

Fig. 6 shows the surface composed by power values obtained with equations in TABLE II for every specific D_1-D_2-φ set. Maximum output power, P_{max}, occurs at $D_1 = D_2 = 1$ and $\varphi = \pi/2$, that corresponds to SM3*, in Fig. 5, and Fig. 6.

The conduction losses reduction is approached from a minimization in the RMS current through the upper inductor, i_{L1}. In [13]–[15] the possibility of operating with minimum RMS i_{L1} for any load is considered. Thanks to the flexibility offered by the number of control parameters in TPS modulation, there are several parameters set D_1-D_2-φ that get the same power value, with different rms i_{L1} value.
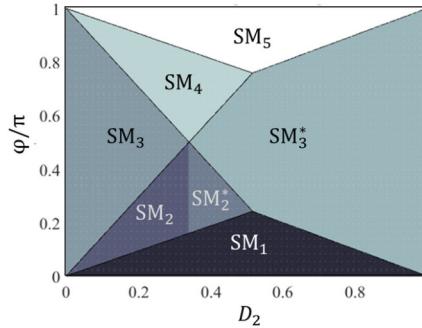

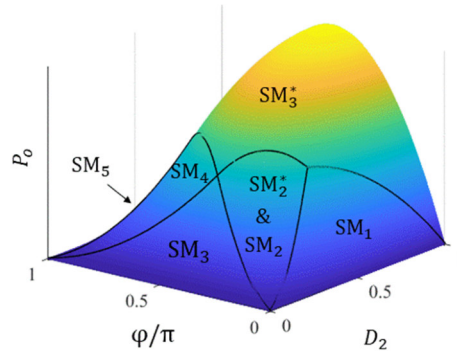Fig. 5 Switching Mode distribution map applied (10) for a given V_1/V_2

Fig. 6 Power surface for the proposed converter in Case 3

To clarify this concept, Fig. 7 shows two 3D plots (D_2-P_o-φ and D_2-$i_{L1,rms}$-φ). The colored cut-lines in both pictures represent surfaces with the same power. A curve made by specific operating points D_1-D_2-φ follows the minimum of each cut-line in the surface composed by D_2-$i_{L1,rms}$-φ. The black curve in plots of Fig. 7 corresponds to the Minimum RMS current path found.
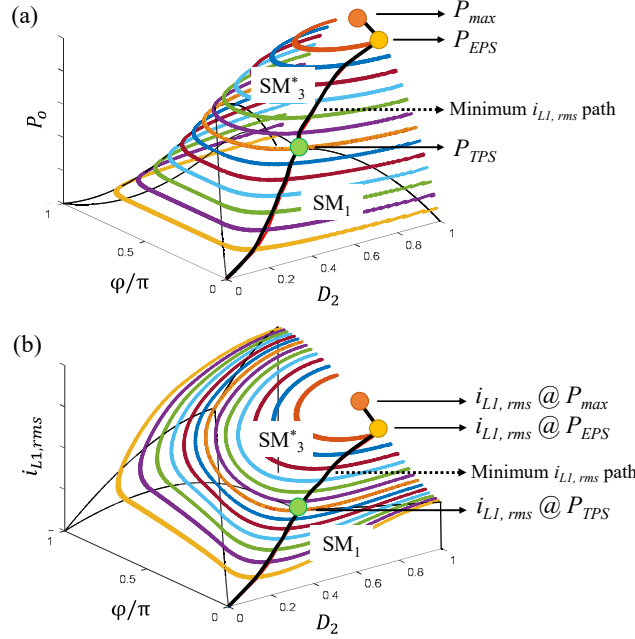

Fig. 7 Constant power surface cuts for (a) power surface and (b) $i_{L1,rms}$ current surface, for proposed converter in *Case 3*

The green and yellow dots on the surfaces of Fig. 7, P_{TPS} and $P_{EPS,}$ identify the power values when the modulation pattern changes from fully TPS to the equivalent EPS pattern (P_{TPS}), and from EPS equivalent pattern to PS pattern (P_{EPS}). Although it is not mandatory to impose P_{TPS} and P_{EPS} as step values to the algorithm, it helps the accuracy of found path solution for larger grid step sizes.

P_{TPS} limit is obtained by substituting the proper values of D_1-D_2-φ_{TPS} at the power expression of SM_1 (TABLE II). Phase shift angle φ_{TPS} is calculated from the upper limit equation of SM_1; D_1 at P_{TPS} is 1, and D_2 is obtained from (10).

P_{EPS} points to the end of the EPS pattern and the start of the PS equivalent pattern. To find it: first, being D_1 equals 1, the φ_{EPS} expression is derived as a function of D_2 and P_o from SM_3* power expression (TABLE II).

Next, φ_{EPS} is replaced into the correspondent i_{L1rms} expression for SM_3*, which is found following the procedure described in Section III. The $i_{L1,rms}$ expression is then derived for D_2 and equalized to zero, to obtain the curve made of all the operating points with minimum $i_{L1,rms}$ in the EPS equivalent pattern. Finally, P_{EPS} is calculated particularizing the result for $D_2 = 1$. The described procedure is based on the proposal in reference [15] for the traditional DAB converter.

Equations (11) and (12) are the expressions of P_{TPS} and P_{EPS}, found following the described procedure for MCB[3] in *Case 3*, with P_b and r defined by (13) and (14), respectively.

$$P_{TPS} = (P_b/r) \cdot (r - 1)/2 \tag{11}$$

$$P_{EPS} = 0.5 \cdot (-P_b \cdot r) \cdot \left(r^2 - 1 - r\sqrt{r^2 - 1}\right) \tag{12}$$

$$P_b = V_1^2/(2 \cdot L \cdot f_{sw}) \tag{13}$$

$$r = V_2/V_1 \tag{14}$$

Fig. 8 shows the simplified algorithm flowchart proposed to find the preferred Minimum rms current path operating points. This off-line algorithm results in a Look-Up Table (LUT) compose of the surfaces of values P_i-D_1-D_2-φ with as many power steps (P_i) as the user sets for the range of voltages settled by the specification requirement. The optimal values of D_1-D_2- φ for any load that does not appear in the table are obtained by interpolation. The use of the proposed search algorithm or simplified equations [16] instead of the exact analytical solution saves computational resources in the case the input specification changes, as the theoretical equations for the Minimum rms current path changes with it. If the grid step size is small enough, the difference between theoretical and the computed Minimum rms current Path is negligible.

Although the MCB[3] converter close-loop design is beyond the scope of this work, the steps for getting the output voltage control are briefly summarized. The algorithm generates off-line the LUT with the data of the control variables, obtained along the Minimum rms current Path, for a specification V_1-V_2-P_{max}. The V_1 and V_2 voltages and the output current are sensed. The compensator processes the error between V_2 and the voltage reference. The compensator output value is multiplied by the sensed

output current to generate P_i. The triad V_1-V_2-P_i is used to consult the LUT and obtaining D_1-D_2-φ. Possible changes to the input voltage, V_1, are solved by having a surface of multiple Paths dependent on V_1, in the LUT.
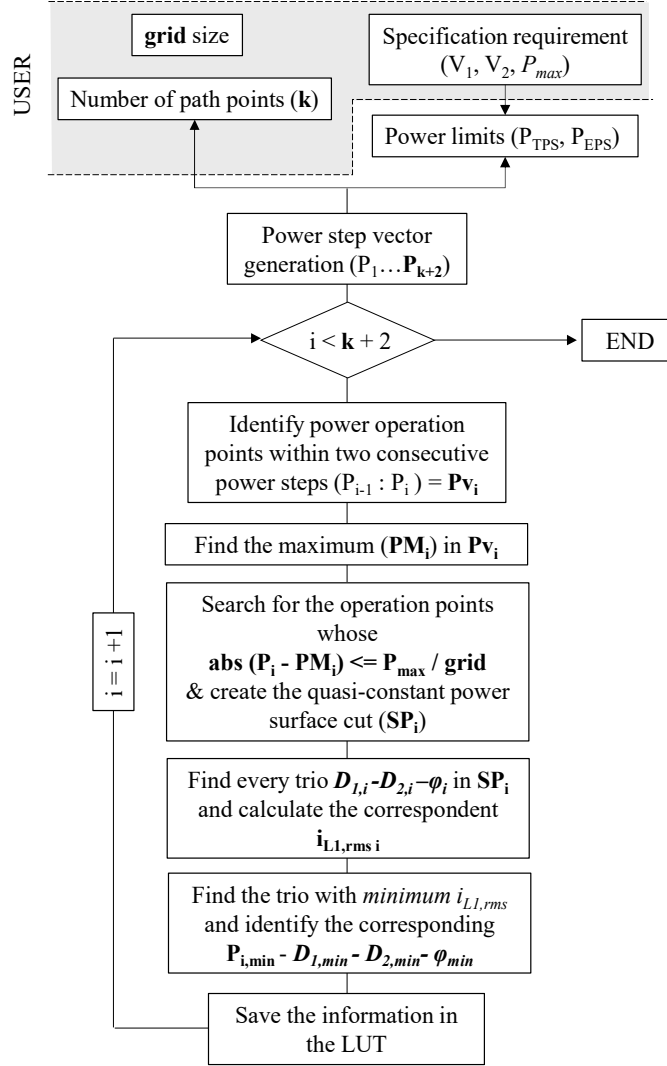

Fig. 8 Minimum $i_{L1,rms}$ path search algorithm flowchart

An increase in L_1 due to the leakage inductance of the CM transformer will reduce the maximum achievable output power, as can be seen in TABLE III. There will also be changes in the power and RMS current surfaces, both dependent on L_1. Therefore, the control parameters D_1-D_2-φ must be recalculated following the procedure described to transfer the same power, reaching a new minimum RMS current. Soft switching is not affected by a change in the value of L_1 according to the equation (10) until P_{TPS} neither after that according to the state of the art [12].

V. VOLTS PER SECOND AT THE CM TRANSFORMER

Until this point, the study of the proposed converter has been based on the consideration of an ideal coupling in the CM transformer that prevents the current returning through the ground line between the two bridges. For the actual case, in which the coupling is not perfect, the L_m value must be controlled so that the ground line current is limited to a small enough value to have a negligible impact on the ideal analysis accomplished.

The volts·second in the MCB³ CM transformer windings are analyzed over the Minimum rms current path operating points, to find a generic equation that helps the transformer sizing, as the volts·second applied to the windings are related with the magnetizing inductance L_m.
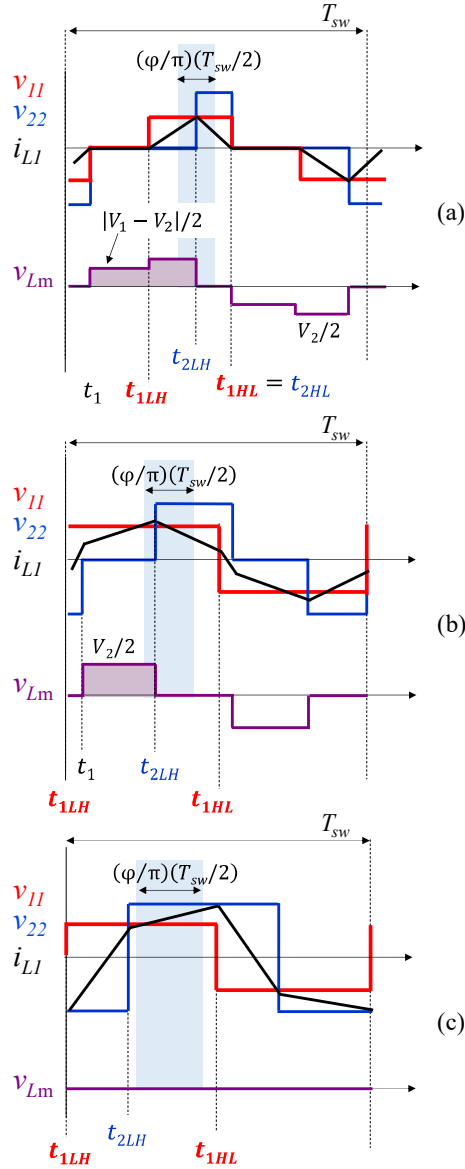
Fig. 9 Volts·second study on the CM transformer over the three equivalent TPS modulation patterns (a) fully TPS, (b) EPS, and (c) (PS).

Fig. 9 shows three generic operating points for the MCB[3] in *Case 3*, belonging to the preferred Minimum rms current Path: TPS modulation in Fig. 9 (a), EPS modulation in Fig. 9 (b), and PS modulation in Fig. 9 (c) equivalent patterns, respectively. The colored area represents the volts·second on the CM transformer windings. As seen, the MCB[3] CM transformer voltage, v_{Lm}, is positive when v_{11}, v_{22}, or both are zero.

As shown in Fig. 9 (a), in TPS there is a considerable amount of time with $v_{11} = v_{22} = 0$. Therefore, the V·s area will be higher than in the rest of the operating points shown. In Fig. 9 (b), with an EPS pattern, the V·s applied is smaller than in Fig. 9 (a), since one of the duty cycles is 1. In Fig. 9 (c) the value of V·s applied is 0 since there are no periods with zero volts in v_{11} and v_{22}.

Volts·second on a magnetic component windings are obtained applying (15) to the positive part of the voltage waveform.

$$\lambda = \int_{t_a}^{t_b} v_{Lm}(t) \; dt \qquad (15)$$

The integration limits t_b and t_a must be replaced by the corresponding values of the switching instants that delimit the waveform v_{Lm}. The process may involve partial integration. Equation (16) is derived for the analyzed *Case 3* and is also valid for *Case 2* if the absolute value is taken.

The maximum value, $\lambda_{MCB^3,max}$, needed to size L_m is reached at $D_1 = D_2 = 0.5$

$$\lambda_{MCB^3,Case\ 3} = \frac{T_{sw}}{2}\left(-v_{C1}(1-D_1) + \left(\frac{V_1}{2} - v_{C1}\right)(D_1 - D_2)\right) = \frac{T_{sw}}{4}\left(V_2(1-D_2) - V_1(1-D_1)\right) \qquad (16)$$

In this work, the volts-second in the transformer windings of the traditional DAB converter is also considered, to evaluate the impact in terms of volume that would imply the construction of a component with the magnetizing current peak limited by a sufficiently large L_m value. For the DAB converter with the same modulation strategy applied, (17) is the expression for the volts·second in the galvanic isolation transformer windings, as v22 will be imposed directly on the isolation transformer windings. In this case, the maximum value, $\lambda_{DAB,\ max}$, occurs in the PS equivalent pattern at high load.

$$\lambda_{DAB} = \frac{D_2 \cdot (V_2/n)}{2 f_{sw}} \qquad (17)$$

Fig. 10 shows the region where $\lambda_{MCB^3,max}$ is smaller than $\lambda_{DAB,max}$, shadowed area. It can be seen that for any voltage ratio, $\lambda_{MCB^3,max}$ is smaller than $\lambda_{DAB,max}$ for the same combination V_2/V_1 and $n = 1$, which is the turns ratio for the MCB^3 converter's CM transformer. This assertion has a limit at $V_2/V_1 = 1/3$, but it will never correspond to the worst-case design at boost operation, then it will not impact on the final power stage design.

VI. TOPOLOGY VALIDATION

In this section, simulation and experimental results are provided to validate the MCB^3 converter theoretical analysis, and to demonstrate that the same enhanced features are achieved by using the described control strategy with DAB and MCB^3 converters. Parameters on TABLE IV are set for both converters to check the behavioral equivalency. Those parameters MCB^3 in bold are the same for both topologies.

The operation in *Case 3* described is validated with voltage ratios $V_2/V_1 > 1$, which includes the worst-case operation.

A magnetizing current peak, Δi_{Lm}, of 0.05A is taken as a common criterion to design the transformer in both converters, small enough to analyze the MCB^3 converter ideally.
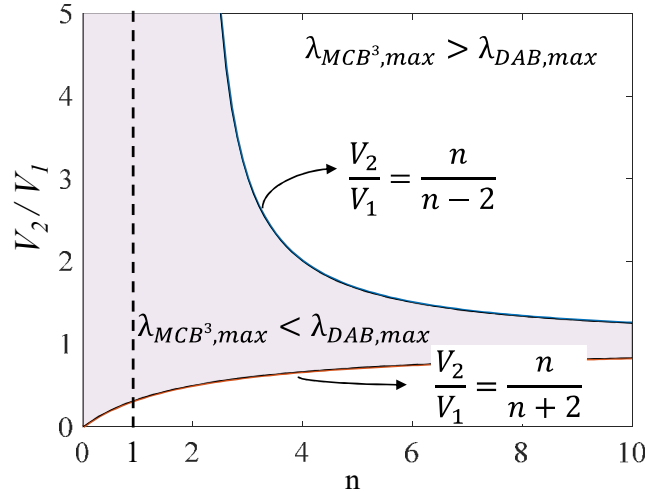

Fig. 10 Maximum volts·second area comparison for MCB^3 CM transformer (λ_{MCB^3}) and DAB transformer (λ_{DAB})

TABLE IV
SPECIFICATION PARAMETERS

Parameter	Topology	Value
V_1		**[124, 278] V**
V_2		**240 V**
P_{max}	DAB and MCB^3	**460 W**
f_{sw}		**50 kHz**
n		**1**
$L_1 = L_2$		80 µH
L_m	DAB/MCB^3	24 mH /5.8 mH
$C_1 = C_2$	MCB^3	14 µF

Equation (18) is used to size L_m to keep Δi_{Lm} limited at the desired value, substituting the term λ_{max}, with the maximum from (16).

$$L_m = \frac{\lambda_{max}}{2 \cdot \Delta i_{Lm}} \qquad (18)$$

The value $L_1 = L_2$ is obtained from the power equation of the Switching Mode SM₃* in TABLE II, to get P_{max} at $D_1=D_2=1$, and $\varphi/\pi = 0.5$. The values are the same for both topologies since the power equations are also the same [16].

The value $C_1 = C_2$ is chosen so that the resonance frequency with the inductances L_1 and L_2, which operate in series, is far away from the switching frequency (at least two decades lower). That way, the impedance of the *AC-link* remains strongly inductive at the switching frequency, getting the intended operation.

A. Simulation results

The simulation of three different operating points belonging to the different modulation patterns (fully TPS, EPS, and PS) in the Minimum rms current path is shown in Fig. 11. Each image shows differential full-bridge voltages v_{11} and v_{22}; i_{L1} current in the proposed MCB³ and the DAB converters, and magnetizing current i_{Lm} in both transformers. The operating points are for 166 W, 333 W, and 460 W (P_{max}). Simulation entries are those from TABLE IV, which reproduce the worst-case design, then V_1 and V_2 are 124 V and 240 V respectively (*r = 1.93*).

The control parameters (D_1-D_2-φ) to simulate the chosen operating points with the expected rms inductor current are shown in TABLE V. Equations to calculate rms i_{L1} (19) and (20) are derived from the procedure described in Section III.

TABLE VI shows the time instants when the MCB³ MOSFETs are turned on and off, and the soft-switching type during turning on. MOSFETs in red are located in Bridge 1, whereas those in blue are in Bridge 2. MOSFETs S_2, S_3, S_5, and S_8 have ZVS, during turning on, when the inductor current, i_{L1}, is positive, or ZCS in case it is zero. In turn, S_1, S_4, S_6, and S_7 have ZVS, during turning on, when i_{L1} is negative, or ZCS in case it is zero.

TABLE VI eases the identification of the soft switching type in the simulation waveforms of Fig. 11, as the turn-on and off instants are described with the *Reference switching instants* indexes. These indexes are self-explanatory of the instant when they occurred, as explained in Section III.

The TPS operating point in Fig. 11 (a), has D_1 and D_2 smaller than 1, with time intervals where $v_{11} = v_{22} = 0$, and corresponds to an SM₁. MCB³ and DAB currents i_{L1} are superimposed. This means that TPS modulation shapes the current profile the same for both topologies, so the same benefits will be obtained from its appliance.

TABLE V
SIMULATION PARAMETERS

Output power	SM	D_1	D_2	φ/π	$i_{L1,rms}$
166 W	SM₁*	0.82	0.43	0.19	1.7 A
333 W	SM₃*	1	0.62	0.28	2.9 A
500 W	SM₃*	1	1	0.5	5.2 A

TABLE VI
SWITCHING TIME AND SOFT SWITCHING IN THE MOSFETs

Switch	Turn-on time	Soft Switching SM₁	Soft Switching SM₃*	Turn-off time	Soft Switching SM₁	Soft Switching SM₃*
S_1	t_{1LH}	ZCS	ZVS	$t_{1LH} + T_{sw}/2$	ZCS	HS
S_2	$t_{1LH} + T_{sw}/2$	ZCS	ZVS	t_{1LH}	ZCS	HS
S_3	t_{1HL}	ZCS	ZVS	$t_{1HL} + T_{sw}/2$	ZCS	HS
S_4	$t_{1HL} + T_{sw}/2$	ZCS	ZVS	t_{1HL}	ZCS	HS
S_5	t_{2LH}	ZVS	ZVS	$t_{2LH} + T_{sw}/2$	HS	HS
S_6	$t_{2LH} + T_{sw}/2$	ZVS	ZVS	t_{2LH}	HS	HS
S_7	t_{2HL}	ZCS	ZVS	$t_{2HL} + T_{sw}/2$	ZCS	HS
S_8	$t_{2HL} + T_{sw}/2$	ZCS	ZVS	$t_{1LH} + T_{sw}/2$	ZCS	HS

$$i_{L1}{}^2{}_{rms,SM1} = \frac{2}{T_{sw}} \int_{t_{1LH}}^{t_{1HL}} i_{L1,SM1}(t)^2 \, dt \ =$$

$$= [D_2^3 V_1 V_2 - 2D_1^3 V_1^2 + 3D_1^2 V_1^2 + 3D_1^2 D_2 V_1 V_2 - 6D_1 D_2 V_1 V_2 + 12D_1 V_1 V_2 \varphi^2 - 2D_2^3 V_2^2 + 3D_2^2 V_2^2] \cdot \frac{1}{48 f_{sw}^2 \cdot (L_1 + L_2)^2} \qquad (19)$$

$$i_{L1}{}^2{}_{rms,SM3*} = \frac{2}{T_{sw}} \int_{t_{1LH}}^{t_{1HL}} i_{L1,SM3*}(t)^2 \, dt \ =$$

$$= [3D_1^2 V_1^2 - 2D_1^3 V_1^2 - 6D_1^2 V_1 V_2 \varphi + 3D_1^2 V_1 V_2 + 12D_1 V_1 V_2 \varphi - 6D_1 V_1 V_2 - 2D_2^3 V_2^2 - 6D_2^2 V_1 V_2 \varphi + 3D_2^2 V_1 V_2 + 3D_2^2 V_2^2 + 12D_2 V_1 V_2 \varphi$$

$$- 6D_2 V_1 V_2 - 8V_1 V_2 \varphi^3 + 12V_1 V_2 \varphi^2 - 12V_1 V_2 \varphi + 4V_1 V_2] \cdot \frac{1}{48 f_{sw}^2 \cdot (L_1 + L_2)^2} \qquad (20)$$
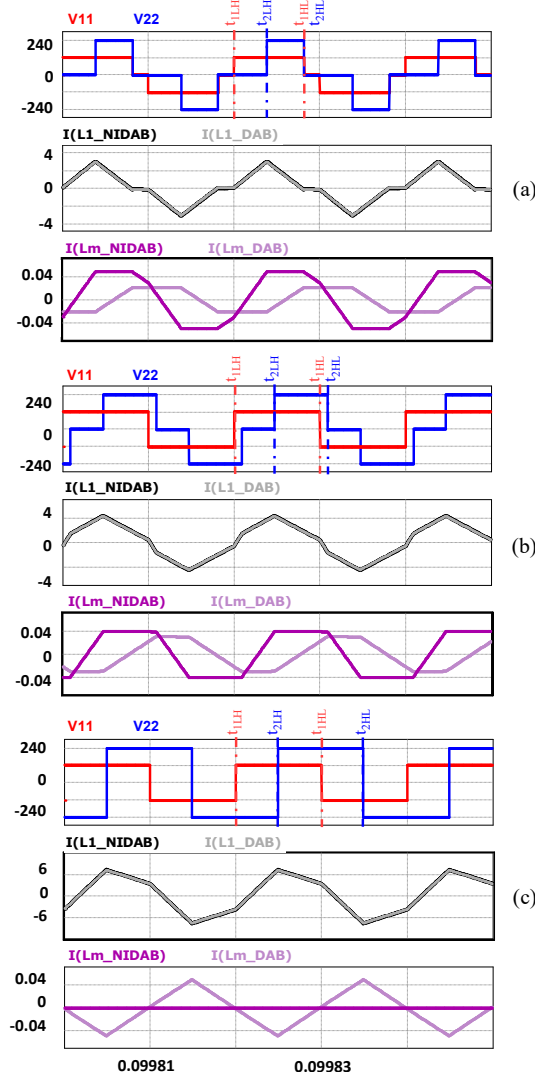

Fig. 11 Simulated waveforms for MCB[3] and DAB converters for (a) TPS at 166 W, (b) EPS at 333 W and (c) 460 W (P_{max}) at PS

Thus, the proposed MCB[3] converter has soft-switching in all the MOSFETs and the minimum rms current for this power requirement. The represented operating point always has non-zero volts·second applied to the CM transformer windings during the switching period. As D_1 and D_2 are related by (10) during pure TPS, then $\lambda_{MCB}{}^3$ remains at a constant value of 0.6 µV·s for any load below P_{TPS}. During this power range, $\lambda_{MCB}{}^3$ reaches the maximum, $\lambda_{MCB}{}^3{}_{,max}$. As seen, Δi_{Lm} reaches 0.05 A at $\lambda_{MCB}{}^3{}_{,max}$; then L_m sizing is validated.

Fig. 11 (b) shows an EPS equivalent pattern operating point. In this case, the current profile belongs to the SM3*. i_{L1} in MCB[3] and DAB converters are superimposed, then the modulation strategy will work the same for both converters, getting soft-switching

and minimum RMS current again in all the MOSFETs. MCB[3] and DAB behavioral equivalency is also verified with EPS modulation.

Fig. 11 (c) shows the PS operating point at P_{max}. The current profile also belongs to the SM$_3$*. Even at PS, i_{L1} of both converters are superimposed so, behavioral equivalency with the traditional DAB converter is verified for every modulation scheme tried, and therefore, for the TPS chosen strategy, which combines all the three patterns. As shown in Section V, DAB magnetizing current peak at 0.05 A is at PS equivalent pattern, and zero at the MCB[3], in the same situation. Therefore, the L_m sizing is validated for any load and topology.

B. Experimental results

A prototype of the proposed MCB[3] converter has been built and tested along with a prototype of the DAB converter to validate the theoretical analysis and simulation, for the specification values of TABLE IV. Both converters have been built using the same layout and same common components (semiconductors, drivers, input and output capacitors, L_1 and L_2 inductors), so the differences are due to the DC blocking capacitors combined with the CM transformer in MCB[3] *AC-link*, compared to the DAB isolation transformer.

The design of the magnetic components follows the standard procedure described in [19], so that the minimum total losses are obtained by finding the optimal flux density for each core size considered. This procedure is applied over the Ferroxcube core database [21], for 3F3 ferrite. Fig. 12 shows the design solutions that comply the basic limitations of window area occupation (set to be less than or equal to 35% as it is handmade) and current density (set to be around 10 A/mm^2). Solutions are located regarding their total magnetic loss in Watts (Y-axis) compare to their effective volume in cubic millimeters (X-axis). Blue dots correspond to the DAB transformer design, purple dots are for MCB[3] CM transformer, and green ones are for inductor L_1. The same inductor design is chosen for the two topologies, as the maximum current and volts·second applied to them are the same. The building parameters are shown in TABLE VII.

In Fig. 13 (a), the full prototype is shown. The promising possibilities for magnetics volume reduction of the proposed MCB[3] converter are highlighted in Fig. 13 (b).
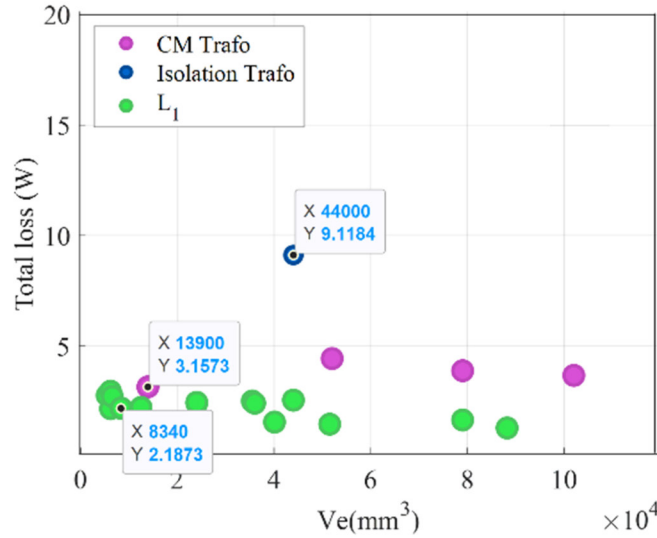

Fig. 12 Magnetic components design considered

TABLE VII
MAGNETIC COMPONENTS BUILDING PARAMETERS

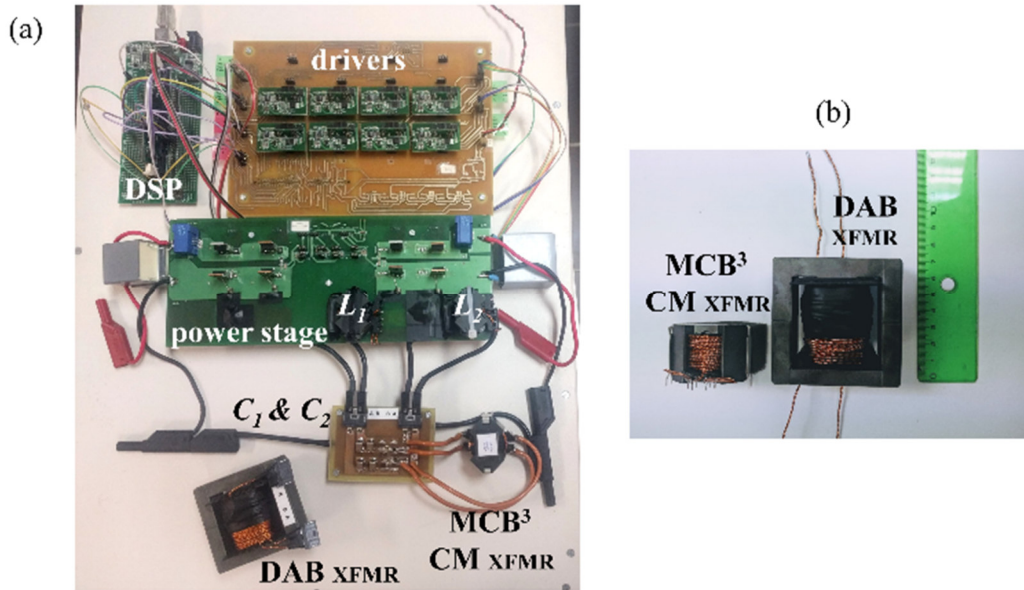| Component	Core	Value	Wire section	N_1/N_2	gap
$L_{m,\ DAB}$	E65/32/27	24.5 mH	3x 0.5mm^2	53/53	-
$L_{m,\ MCB}$[3]	RM14	5.6 mH	3x 0.5mm^2	30/30	-
$L_1 = L_2$	RM12	80µH	3x 0.5mm^2	28	1.9mm

Fig. 13 Pictures of (a) experimental prototype set-up, and (b) detail of MCB^3 and DAB transformers

The CM transformer is six times smaller than the DAB isolation transformer. The sum of the DC blocking capacitors (KRM55WR72A226MH01L) and the CM transformer volumes represents 18% of DAB's transformer volume. Then, although it is possible to use the DAB converter in non-isolated applications, the proposal saves volume while maintaining the same preferable features.

The measurements on MCB^3 and DAB prototypes are shown in Fig. 14. Images (a) to (c) correspond to the MCB^3 converter, and images (d) to (f) to the DAB. The measurements are done for the operating points in TABLE V to check whether the experimental results agree with the simulations.

Differential voltages v_{11} and v_{22} are shown in yellow and grey using the same scale, displayed as *Math1*. Inductor current, i_{L1}, is shown in channel *Ch3* in purple. *Reference switching instants* are shown with a red line (continuous at t_{1LH} and dashed at t_{1HL}) for Bridge 1, and in blue (continuous at t_{2LH} and dashed at t_{2HL}) for Bridge 2.

TPS operating point is shown in Fig. 14 (a), for the MCB^3 converter and in Fig. 14 (d) for the DAB converter.

As can be seen, the waveforms are much alike to those expected from the corresponding simulation results, in Fig. 11 (a).

The EPS equivalent pattern operating point is shown in Fig. 14 (b) and Fig. 14 (e), for the MCB^3 converter and the DAB converter, respectively. The waveforms are practically identical to those expected from the corresponding simulation, Fig. 11 (b).

The current peak of 4.5A is a little higher than obtained in simulation (Section 4.2 A) as the losses are compensated for having the exact output voltage value.

TPS operating point is shown in Fig. 14 (a), for the MCB^3 converter and in Fig. 14 (d) for the DAB converter. As can be seen, the waveforms are much alike to those expected from the corresponding simulation results, in Fig. 11 (a).

The EPS equivalent pattern operating point is shown in Fig. 14 (b) and Fig. 14 (e), for the MCB^3 converter and the DAB converter, respectively. The waveforms are practically identical to those expected from the corresponding simulation, Fig. 11 (b).

The current peak of 4.5A is a little higher than obtained in simulation (4.2 A) as the losses are compensated for having the exact output voltage value.

P_{max} current profiles in Fig. 14 (c) and Fig. 14 (f) belongs to SM$_3$*. As the last operating point considered, it finishes with the validation of current waveform matching between MCB^3 theoretical analysis, simulation study, and experimental measurements.

The behavioral equivalency of the proposed MCB^3 converter with traditional DAB converter is also wholly verified, as their current profiles match for any load and modulation pattern considered. This feature allows the MCB^3 converter to be further enhanced with any other contributions done in the research for the DAB converter [20].
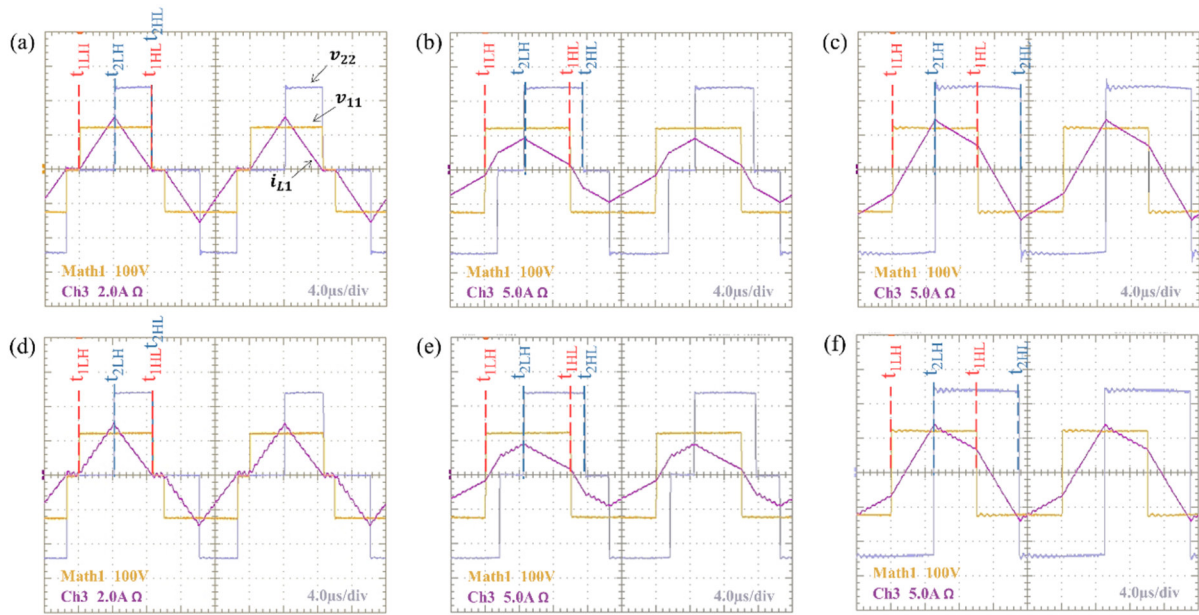
Fig. 14 Experimental results of 166W, 333W, and P_{max} for the MCB^3 converter (a to c) and for the DAB converter (d to f)

Fig. 15 shows the efficiency curves of the proposed MCB^3 converter for three different V_1 voltages within the range indicated in TABLE IV. A maximum efficiency of 95.2% has been reached in the worst-case design (highest V_2/V_1 ratio, blue curve), and 97.2% for 200V to 240V (input voltage to output voltage, orange curve) for the TPS operation described.

The differences are especially noticeable from medium to high load, where conduction losses become more relevant. Since the current to provide the same output power is reduced as the input voltage increases, the losses are lower as well.

In addition, Fig. 15 shows P_{TPS} (green dot) and P_{EPS} (orange dot) occurrence for the MCB^3 converter at the 124V-240V efficiency curve. These dots correspond to the ones shown in Fig. 6.

The traditional DAB converter and MCB^3 efficiency curves for the highest V_2/V_1 ratio (124V – 240V) are shown in Fig. 16, for the same TPS operation and the parameters in TABLE IV. The red crosses point out the waveforms shown in Fig 14.

The difference in the efficiency between the MCB^3 converter and the DAB converter curves for all power range is due to the DAB transformer's bigger volume. As the magnetizing current peak is fixed by design, core loss depends only on the volume. The efficiency drop in both curves occurs after the Switching Mode region change from SM$_1$ to SM$_3$*, as the number of MOSFETs with Hard Switching turning off increases, as shown in TABLE VI .
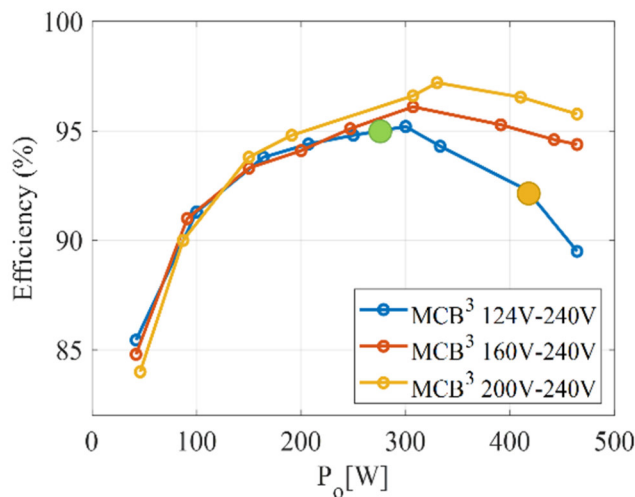

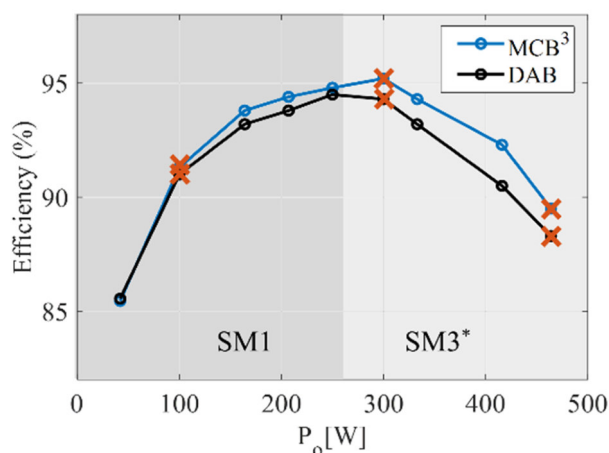Fig. 15 MCB^3 converter efficiency curves at different input voltages

Fig. 16 MCB^3 and DAB converters efficiency curves at V_1=124V and V_2=240V

VII. Conclusions

A novel buck-boost bidirectional non-isolated topology named Magnetically Coupled Buck-Boost Bidirectional converter (MCB^3) is presented.

The proposed converter gets soft-switching operation, with no need for variable frequency or snubbers, over the entire load range. The MCB^3 converter operation resembles the one of popular DAB converter, exploiting the AC power transfer operation and getting to better use of the magnetic elements. Thus, the MCB^3 is focused on those applications fields that do not require high-level safety, and therefore do not need galvanic isolation, but in which having the main features of the DAB is an advantage.

Triple Phase Shift (TPS) modulation is used on the MCB^3 converter for taking advantage of this operation equivalency, as it allows achieving not only the soft-switching operation but also minimum rms current for any power requirement.

The steady-state analysis of the proposed converter and the procedure to derive the rms current expressions is described. General soft-switching operation condition and the procedure to find the Minimum rms current path are also provided. The optimal control parameters to achieve the preferred operation are shown.

The volts·second in the Common Mode transformer windings are studied to analyze the magnetic integration possibilities. The volts·second in the DAB converter isolation transformer are considered to emphasize the volume reduction in the proposal when the evaluated components are built to have the same magnetizing current peak. Maximum volts·second in CM transformer remains smaller than those in the DAB isolation transformer for buck-boost voltage gain ratios from 1/3 to 3, providing the turns ratio in the DAB converter is chosen to meet the voltage ratio, as it is commonly recommended to achieve better performance [12].

The simulation results validate the behavioral equivalency of the proposed converter with a traditional DAB converter, for any load and modulation pattern considered during the control strategy used. The prototypes of the MCB^3 and DAB converters are build and tested, sharing the full bridges and the input and output filters to evidence the proposal contributions. MCB^3 converter efficiency remains equal or higher than the DAB's one, with a maximum of about 95%, which is in the same order as the better topology considered in the state-of-art initial research. The passive components total volume in the proposed MCB^3 converter is around 1/5 of those in the DAB converter.

Besides, it is expected that the particularity of the MCB^3 converter to replicate the DAB operation will allow it to improve its performance with other contributions developed for the DAB converter.

References

[1]   Y. Du, X. Zhou, S. Bai, S. Lukic, and A. Huang, "Review of non-isolated bi-directional DC-DC converters for plug-in hybrid electric vehicle charge station application at municipal parking decks," *Conf. Proc. - IEEE Appl. Power Electron. Conf. Expo. - APEC*, no. 1, pp. 1145–1151, 2010.

[2]   M. Bragard, N. Soltau, S. Thomas, and R. W. De Doncker, "The balance of renewable sources and user demands in grids: Power electronics for modular battery energy storage systems," *IEEE Trans. Power Electron.*, vol. 25, no. 12, pp. 3049–3056, 2010.

[3]   M. Kasper, D. Bortis, and J. W. Kolar, "Classification and comparative evaluation of PV panel-integrated DC-DC converter concepts," *IEEE Trans. Power Electron.*, vol. 29, no. 5, pp. 2511–2526, 2014.

[4]   K. Tytelmaier, O. Husev, O. Veligorskyi, and R. Yershov, "A review of non-isolated bidirectional dc-dc converters for energy storage systems," *Proc. Int. Young Sci. Forum Appl. Phys. Eng.*, no. November 2017, pp. 22–28, 2016.

[5]   K. Thirugnanam, S. K. Kerk, C. Yuen, N. Liu, and M. Zhang, "Energy Management for Renewable Microgrid in Reducing Diesel Generators Usage with Multiple Types of Battery," *IEEE Trans. Ind. Electron.*, vol. 65, no. 8, pp. 6772–6786, 2018.

[6]   I. D. Kim, S. H. Paeng, J. W. Ahn, E. C. Nho, and J. S. Ko, "New bidirectional ZVS PWM sepic/zeta DC-DC converter," *IEEE Int. Symp. Ind. Electron.*, no. 3, pp. 555–560, 2007.

[7]   B. Ulrich, "Analysis of a zvs synchronous sepic/zeta dc/dc converter," *PCIM Eur. Conf. Proc.*, no. 225809, pp. 1623–1630, 2018.

[8]   X. Weng *et al.*, "Comprehensive comparison and analysis of non-inverting buck boost and conventional buck boost converters," *J. Eng.*, vol. 2019, no. 16, pp. 3030–3034, 2019.

[9]   S. Waffler and J. W. Kolar, "A Novel Low-Loss Modulation Strategy for High-Power Bidirectional Buck Boost Converters," *Power Electron. IEEE Trans.*, vol. 24, no. 6, pp. 1589–1599, 2009.

[10]   X. F. Cheng, Y. Zhang, and C. Yin, "A Zero Voltage Switching Topology for Non-inverting Buck-Boost Converter," *IEEE Trans. Circuits Syst. II Express Briefs*, vol. PP, no. c, p. 1, 2018.

[11]   A. Amin, M. Shousha, A. Prodic, and B. Lynch, "A transformerless dual active half-bridge DC-DC converter for point-of-load power supplies," *2015 IEEE Energy Convers. Congr. Expo. ECCE 2015*, pp. 133–140, 2015.

[12]   A. Rodríguez, A. Vázquez, D. G. Lamar, M. M. Hernando, and J. Sebastián, "Different purpose design strategies and techniques to improve the performance of a dual active bridge with phase-shift control," *IEEE Trans. Power Electron.*, vol. 30, no. 2, 2015.

[13]   F. Krismer and J. W. Kolar, "Closed form solution for minimum conduction loss modulation of DAB converters," *IEEE Trans. Power Electron.*, vol. 27, no. 1, pp. 174–188, 2012.

[14]   J. Huang, Y. Wang, Z. Li, and W. Lei, "Unified Triple-Phase-Shift Control to Minimize Current Stress and Achieve Full Soft-Switching of Isolated Bidirectional DC-DC Converter," *IEEE Trans. Ind. Electron.*, vol. 63, no. 7, pp. 4169–4179, 2016.

[15]   C. Calderon, A. Barrado, A. Rodriguez, A. Lazaro, M. Sanz, and E. Olías, "Dual Active Bridge with triple phase shift , soft switching and minimum RMS current for the whole operating range," in *IECON - Annual Conference of the IEEE Industrial Electronics Society*, 2017, vol. 11.

[16]   C. Calderon *et al.*, "General Analysis of Switching Modes in a Dual Active Bridge with Triple Phase Shift Modulation," *Energies*, vol. 11, no. 9, p. 2419, 2018.

[17]   B. Zhao, Q. Yu, and W. Sun, "Extended-phase-shift control of isolated bidirectional DC-DC converter for power distribution in microgrid," *IEEE Trans. Power Electron.*, vol. 27, no. 11, pp. 4667–4680, 2012.

[18]   B. Zhao, Q. Song, W. Liu, and Y. Sun, "Overview of dual-active-bridge isolated bidirectional DC-DC converter for high-frequency-link power-conversion system," *IEEE Trans. Power Electron.*, vol. 29, no. 8, pp. 4091–4106, 2014.

[19]   D. M. Robert W.Erickson, *Fundamentals of Power Electronics*, Second. New York: Kluwer Academic Publishers, 2011.

[20]   O. M. Hebala, A. A. Aboushady, K. H. Ahmed, and I. Abdelsalam, "Generic Closed-Loop Controller for Power Regulation in Dual Active Bridge DC-DC Converter With Current Stress Minimization," *IEEE Trans. Ind. Electron.*, vol. 66, no. 6, pp. 4468–4478, 2019.

[21]   Ferroxcube, *Soft Ferrites and Accessories - Data Handbook*. 2013.